CrossMark

Modification of the Shear-Compression Specimen for Large Strain Testing

A. Dorogoy[1] · D. Rittel[1] · A. Godinger[1]

Abstract A modified shear-compression specimen (SCS), for large strain testing over a wide range of strain rates is presented. The original SCS design includes two rectangular slots that are machined at 45° with respect to the longitudinal axis. The modification consists of creating two diametrically opposed semi-circular slots. The new "circular" specimen is first thoroughly investigated numerically under quasi-static and dynamic loading using an elasto-plastic material model. The results of the comparison between the two-slot designs confirm the feasibility of the new specimen for larger strain testing and indicates its advantages over the rectangular slot design: larger strain range characterization, failure and fracture within the gauge, and constant Lode parameter during plastic deformation. Both types of SCS as well as cylindrical specimens are used to characterize the flow behavior of steel 1020, in the quasi-static and dynamic regimes using a split Hopkinson pressure bar. Dog-bone specimens are also tested quasi-statically in tension. A very good agreement is achieved for the results of all specimens in both the quasi-static and dynamic regimes. The numerical validation procedure shows that the flow stress of 1020 steel obtained with the new SCS is ~3 % lower in the quasi-static regime, and 8 % lower in the dynamic regime with respect to the flow stress of the rectangular SCS. This difference is attributed to effect of the third invariant of the stress deviator (i.e., Lode parameter), which is considerably lower in the new SCS design.

✉ A. Dorogoy
dorogoy@technion.ac.il

[1] Faculty of Mechanical Engineering, Technion – Israel Institute of Technology, 32000 Haifa, Israel

Introduction

The shear compression specimen (SCS), has been originally developed in Rittel et al. [1] for large strain testing of materials over a wide range of strain rates. The specimen consists of a cylinder having an inclined gage section created by two diametrically opposed rectangular slots which are machined at 45° with respect to the longitudinal axis.

The specimen was thoroughly investigated under quasi-static [2] and dynamic loading [3], using three-dimensional elasto-plastic numerical simulations in which a bi-linear and a parabolic hardening material model were assumed [4]. These studies confirmed the potential of the SCS for large strain testing of materials over a wide range of strain rates by:

1) Verifying the uniformity of the stresses and strains within the gage.
2) Showing that the averaged Mises stress versus the averaged plastic strain on the mid-section of the gauge represent the characteristic behavior of the material.
3) Showing that a simple formulation can relate the experimentally measured loads and displacements to the equivalent stress and strain characteristics of the material.

The specimen was successively used in numerous investigations, including constitutive testing (e.g., [5–7]), texture evolution (e.g., [8]), and adiabatic shear banding [9–11]. A miniature version of the SCS was used for the characterization of nanomaterials [12], and a modified SCS geometry was developed to investigate the mechanical response of polymers

[13, 14]. An analytical data reduction scheme was proposed by [15].

The shear deformation mode, which is dominant within the gauge section, allows for large strain testing, but the failure of the specimen occurs in the fillet regions where stress concentration exists, as observed in Ref. [16] for adiabatic shear band investigations. Hence, accurate failure parameters cannot be extracted directly from the stress–strain curves which represent the mechanical fields within the gauge section. The early failure in the gauge fillets limits also the range of achievable plastic strains. The fracture location is difficult to predict [17], as it may either be on the upper or the on lower fillets, sometimes even alternating between them.

In this study we introduce a modification to the common SCS specimen which addresses and solves the above mentioned drawbacks. In the modified specimen, the two diametrically machined gauges are now *semi-circular* (instead of rectangular). This modification induces large strains on the mid-section section of the gauge without the sharp edges and stress concentrations of the former rectangular gauges.

The study is divided into three main parts. In the first part, the new specimen is introduced and evaluated numerically in comparison with the rectangular one. In the second part, we confirm the potential of the new specimen experimentally by characterizing the flow behavior of as received cold drawn round 1020 steel bars, subjected to quasi-static and dynamic compression and quasi-static tension. In the third part, the results are validated numerically and comparisons are reported. The results are then discussed and conclusions are drawn in the last section.

Numerical Evaluation of an SCS with Circular Gauge

The numerical analyses were performed with the commercial finite element software Abaqus standard and Abaqus explicit 6.12-2 [18]. The purpose of the numerical simulations is to demonstrate that:

1) The field variables such as Mises stress (σ_{Mises}), pressure and equivalent plastic strain (ε_p^{eqv}) are evenly distributed on the mid section of the circular gauge during the entire loading history.
2) The evolution of the average Mises stress and equivalent plastic strain on the mid section of the circular gauge replicate the material property (which is input to the simulation).
3) Compare the new type of specimen to the older one with a rectangular gauge cross section in terms of stress–strain and failure characteristics assessment.

Geometry

A modified SCS specimen, which differs only by the shape of its gauge was examined numerically. The modified SCS is shown in Fig. 1: A front view is shown on Fig. 1a; A side view in Fig. 1b; A cut view perpendicular to the gauge is shown in Fig. 1c.

The dimensions of the specimen are: H=20[mm], D=10[mm], t=1.6[mm]. The circular gauge has a radius of r=1.5[mm]. The gauge width is W=2r=3[mm]. The vertical height of the gauges is $h = 2\sqrt{2}\,r = 4.24\,[mm]$.

Numerical Model, Mesh, Boundary Conditions and Material Property

Due to symmetry of the specimen, only half of the physical model is included in the numerical model. The meshed computational model is shown in Fig. 2. The front, back and side views are shown in Fig. 2a, b, c respectively. The typical mesh shown in Fig. 2 has 85,901 nodes and 78,800 linear hexahedral elements of type C3D8R. The seed size within the gauge is 0.2 [mm]. A vertical displacement of 4 [mm] was applied on the upper face of the specimen (Fig. 2b). Symmetry conditions were applied along the cut (Fig. 2c) and on the bottom face (Fig. 2b). The center point of the bottom face was fixed (Fig. 2b). When an explicit solution scheme was used, the displacement load was applied "slowly"—during 0.001 [s].

Elasto-plastic material model with Mises plasticity was used for the specimen. The density: 7870 $\left[\frac{Kg}{m^3}\right]$; Young modulus: 210 [GPa]; Poison ratio: 0.3. The flow stress versus the equivalent plastic strain is shown in the sequel (Fig. 7). These properties do not represent a particular steel but are common for steels.

Numerical Results

The deformed specimen with the circular gauge is shown in Fig. 3. The distributions of the equivalent plastic strain and Mises stress are shown on the deformed specimen in Fig. 3a and b, respectively. The deformation and distributions which are shown in Figs. 3 and 4 are typical for large plastic deformations and correspond to applied vertical displacement of d=2.4 [mm] which is applied strain of $\varepsilon_{applied} = \frac{d}{h} = 0.57$.

The results show that the Mises stress and the equivalent plastic strain are distributed quite evenly over a wide portion of the width w. This even distribution indicates a proper choice of dimensional parameters. End effects (shown in Fig. 3a,b) are noticeable on both fillets of the gauge, in which the width of the area of uniform distribution become smaller and inclined upwards on the left and downwards on the right.

Stress and strain distribution along the mid-section of the circular gauge specimen are shown in Fig. 4. The distributions
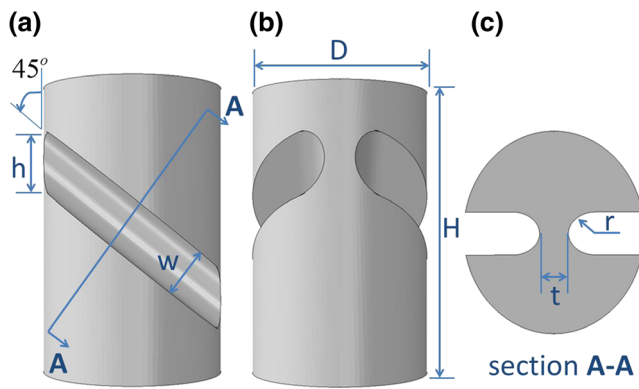
Fig. 1 An SCS specimen with a circular gauge. **a**. Front view **b**. Side view. **c**. A cut view (A-A) perpendicular to the gauge inclination

of the equivalent plastic strain, Mises stress and hydrostatic pressure are shown in Fig. 4a, 4b and 4c respectively. The quite uniform distributions can clearly be observed.

The results of the new SCS were compared numerically to the specimen having a rectangular gauge cross section. The equivalent rectangular type is shown in Fig. 5. All dimensions are identical to those in Fig. 1, except of the rectangular cross section of the gauge which has the same thickness t and width $w=2r$. A small radius of curvature $r_0=0.25$ [mm] exists in the corner.

A ductile failure criterion was added to the analyses of the two types of specimens. According to the failure criterion, an element is failed and deleted when the equivalent plastic strain reaches an arbitrarily set value of $\varepsilon_p^f=1.2$. A vertical displacement of 4 [mm] was applied on the top face of both specimens. Both specimens failed and are shown in Fig. 6. The rectangular type gauge is shown in Fig. 6a and the modified specimen with the circular gauge in Fig. 6b.

The failure patterns of the specimens are different. The rectangular type specimen failed at the corners where stress concentrations exist. A crack started simultaneously on the upper left gauge fillet and the bottom right fillet. The two

cracks propagated towards the mid-gauge and coalesced at the middle by creating an inclined crack segment.

The cracks on the circular type specimen started likewise simultaneously at both ends of the gauge. Their initiation on the left side was a bit above the center line while on the right side a bit below it. They both propagated towards the center of the gauge, approximately at mid-height of the gauge..

The average values on the mid-section were estimated at each time interval by taking the average values of all elements along the two paths shown in Fig. 4a. The average Mises stress (σ_{Mises}) against the averaged equivalent plastic strain (ε_p) for both specimen types are shown in Fig. 7. These values are compared to Abaqus input for the material stress–strain curves. It can be observed that the average values on the mid cut section of both specimens replicate very well the input material behavior (ε_p,σ) which was the input for the analyses.

It can also be observed that the rectangular type specimen failed at $\varepsilon_p \simeq 0.7$ while the circular type failed at $\varepsilon_p \simeq 1.05$, according to the above-mentioned failure criterion. Since the failure strain was set to $\varepsilon_p^f=1.2$, this result means that the rectangular type specimen could characterize the flow behavior of the material only up to 58 % of the failure strain, while the circular type could do it up to 88 % of the failure strain.

Figure 8 shows the applied load-displacement curves (d,p) for both types of specimens. The displacement is normalized by the vertical height of the gauge h and the load by the vertical projection of the area of the mid-cut section ($D \cdot t$). The parameters h, D and t are shown in Figs. 1 and 5. The results indicate that the load to failure of the circular type specimen is 21 % higher than the rectangular one. This is because ε_p^f is 50 % higher for the circular specimen at failure. The applied displacement to failure of both specimens are rather comparable: For the circular specimen, it is ~6 % lower than that of the rectangular one.

The triaxiality (t_r) and the Lode parameter (μ) are defined by Eqs 1–2 ([19, 20]) as:

$$t_r = \frac{p}{\sigma_e} \tag{1}$$

$$\mu = \frac{2\sigma_2 - \sigma_1 - \sigma_3}{\sigma_1 - \sigma_3} \tag{2}$$

Where the pressure (p) and the equivalent Mises stress (σ_e) are given in Eqs. 3–5

$$p = -\sigma_m = -\frac{1}{3}\sigma_{ii} = -\frac{1}{3}(\sigma_1 + \sigma_2 + \sigma_3) \tag{3}$$

$$\sigma_e = \sqrt{\frac{3}{2} s_{ij} s_{ij}}$$

$$= \sqrt{\frac{1}{2}\left[(\sigma_1 - \sigma_2)^2 + (\sigma_2 - \sigma_3)^2 + (\sigma_3 - \sigma_1)^2\right]} \tag{4}$$
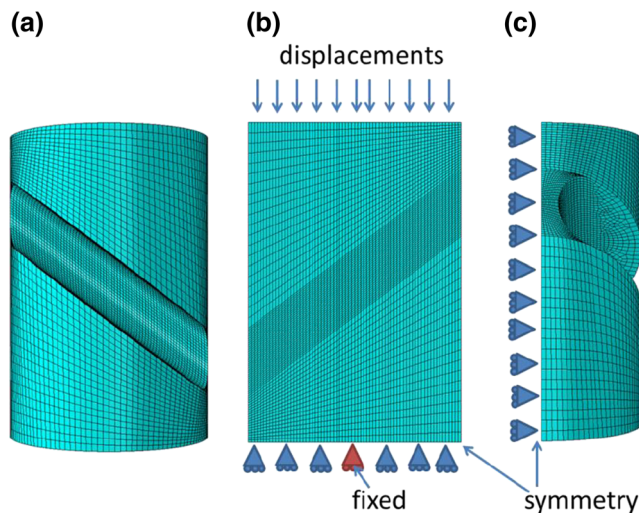
$$s_{ij} = \sigma_{ij} - \sigma_m I \tag{5}$$

Fig. 2 The meshed numerical model. **a**. Front view. **b**. Back view. **c**. Side view

Fig. 3 Distribution of ε_p^{eqv} and σ_{Mises} at applied vertical displacement of $d=2.4$ [mm]. **a**. Front view of a deformed specimen with color maps of ε_p^{eqv}. **b**. A cut view of an un-deformed specimen with color maps of ε_p^{eqv}. **c**. Front view of a deformed specimen with color maps of σ_{Mises}. **d**. A cut view of an un-deformed specimen with color maps of σ_{Mises}
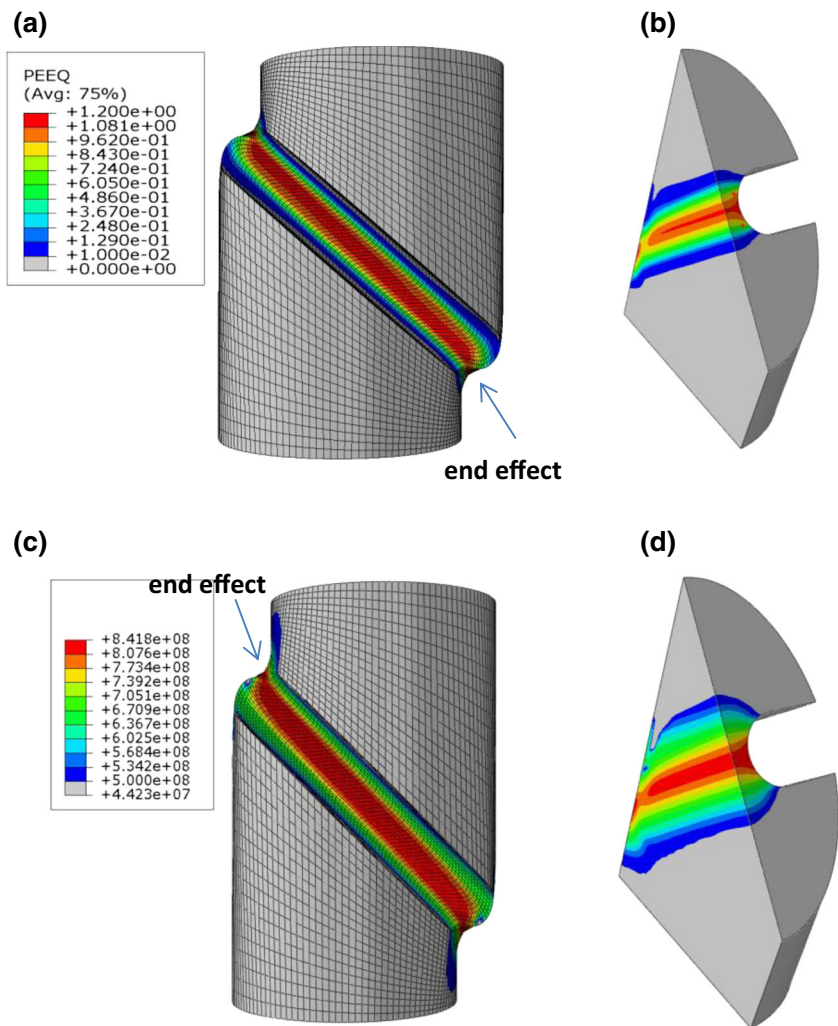
The stresses σ_1, σ_2 and σ_3 are the principal stresses with $\sigma_1 > \sigma_2 > \sigma_3$.

The values of the Lode parameter varies between -1 and 1 ($-1 \leq \mu \leq 1$). Three special cases are associated with the values: $-1, 0$ and 1, which are : generalized tension, generalized shear and generalized compression. The generalized compression case in which $\sigma_1 = \sigma_2$ is illustrated in Fig. 9.

These two parameters are important since they are known to influence the flow behavior and ductility (equivalent plastic strain to failure) of materials [19–24]. Fig. 10 shows the variation of the *averaged* triaxiality and Lode (t_r, μ) parameters during the plastic deformations. The results indicate that the averaged triaxiality (t_r) on the mid-section of both specimens during plastic deformation is quite similar. When the mid-section yields, the triaxiality is ~0.3 and during accumulation of plastic deformation it reduces, reaching ~0.2 at failure.

The behavior of the averaged Lode parameter (μ) on the mid-section of both specimens is quite different.

For the rectangular type specimen it is ~0.9 at yield, decreasing with increasing plastic strain to reach ~0.5 at failure. On the other hand μ of the circular specimen is rather constant and ranges between $0.45 \leq \mu \leq 0.6$.

Constant values of t_r and μ are desirable during the plastic deformation, hence the circular type specimen has a distinct advantage over the rectangular type.

Data Reduction Technique

During an experiment with an SCS, the applied load (P) and vertical displacement (d) are measured, as shown in Fig. 8 from numerical simulations. The goal of the data reduction technique is to transform the measured d-P curve on the specimen face into the characteristic $\sigma_t - \varepsilon_t$ of the material. It was shown that the averaged $\sigma - \varepsilon$ on the mid-section represents well the $\sigma_t - \varepsilon_t$. The procedure is similar to what is detailed in [2–4]. First we map the applied displacement d for $d > d_Y$ into the averaged equivalent plastic strain ε_p (Eq. 6). Next, we

(a)
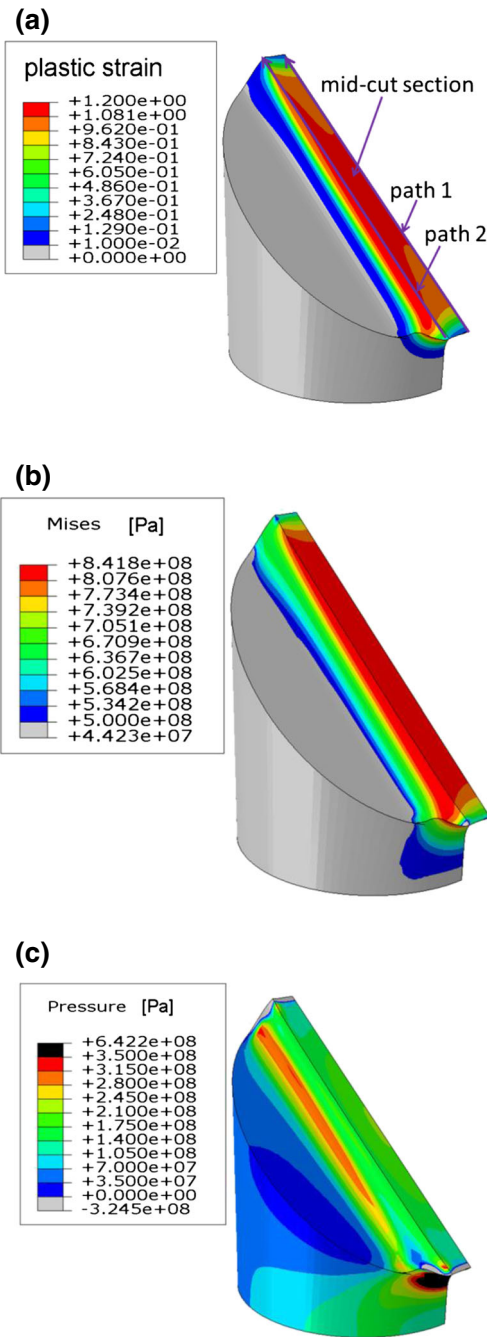

(b)

(c)

Fig. 4 Stress and strain distribution along the mid-section of the circular gauge specimen at vertical applied displacement of 2.4 [mm]. **a**. Equivalent plastic strain distribution. **c**. Mises stress distribution. **d**. Hydrostatic pressure distribution

map the applied load P for $P > P_Y$ into the averaged Mises stress (Eq. 7).

$$\widehat{\varepsilon}_p = \sum_{i=1}^{N} k_{i+2} \left(\frac{d - d_Y}{h} \right)^i \quad for \, d > d_Y \tag{6}$$

$$\widehat{\sigma} = k_1 \left(1 - k_2 \widehat{\varepsilon} \right) \frac{P}{D \cdot t} \quad for \, P > P_Y \tag{7}$$
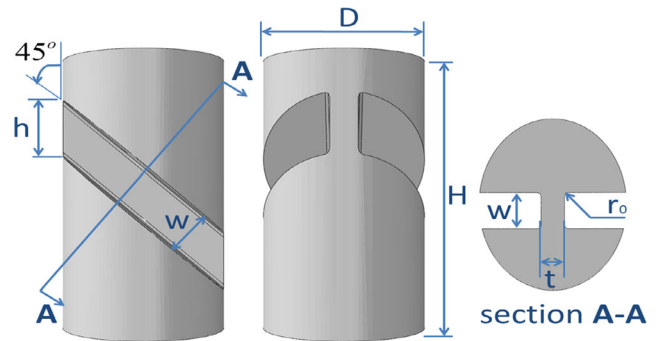
Fig. 5 An SCS specimen with a rectangular gauge. **a**. Front view **b**. Side view. **c**. A cut view (A-A) perpendicular to the gauge inclination

The total strain is: $\varepsilon = \varepsilon_p + \varepsilon_e = \varepsilon_p + \frac{\sigma}{E}$. For most metals the elastic strain is negligible in comparison with the plastic strain $\left(\varepsilon_e << \varepsilon_p \right)$, hence using $\varepsilon \simeq \varepsilon_p$ is justified. The yield point (d_Y, P_Y) on the applied load-displacement curve (P-d), which corresponds to $(\varepsilon_Y, \sigma_Y)$ is shown in Fig. 8.

Figure 11a shows the variation of the averaged plastic strain (ε_p) on the mid-section of the gauge with the applied normalized displacement $\varepsilon = \frac{d}{h}$ for both types of specimens. It can be observed that for the rectangular gauge the dependence is almost linear and an approximation using $N=1$ of the type : $\varepsilon_p = k_3 \frac{d - d_y}{h}$ is sufficient for accurate mapping, as it has been done for example in [1, 5, 7]. For the circular gauge the dependence is clearly nonlinear, hence $N=2$ or 3 must be used for accurate mapping.
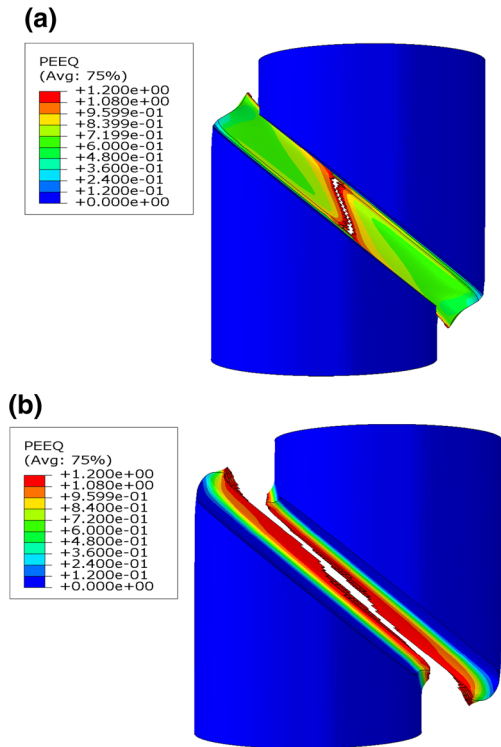
(a)

(b)

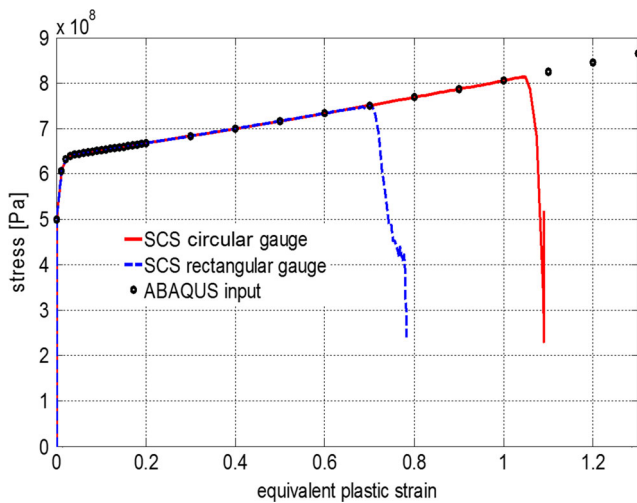**Fig. 6** Failure patterns of specimen. **a**. A rectangular gauge specimen. **b**. A circular type specimen

Fig. 7 Comparison of the averaged values $\left(\varepsilon_p, \sigma_{Mises}\right)$ along the mid-cut section obtained by both types of specimens to the input material property (ε_p, σ) to Abaqus

Figure 11b shows the variation of the averaged Mises stress on the mid-cut section of the gauge with the applied normalized load $\left(\frac{P}{D \cdot t}\right)$. The variation of both specimens is similar. The plastic region for which $(P_Y, \sigma_Y) < (P, \sigma) < \left(P_f, \sigma_f\right)$ where (P_Y, σ_Y) is the yield point and (P_f, σ_f) is the fracture point, is emphasized.

In order to verify the data reduction technique, a 4 [mm] displacement was applied numerically on both types of specimen without using a failure criterion. The reason for that is to avoid setting a limit on the maximum ε_p on the mid-section. A displacement of 4 [mm] resulted in maximum $\varepsilon_p \simeq 1.0$ and $\varepsilon_p \simeq 1.4$ for the rectangular and circular gauge, respectively.

The data reduction technique was utilized with a Matlab [25] user code using least squares. For the circular gauge $N=3$ was used in conjunction of Eq. 6 and for the rectangular gauge $N=1$ and $N=2$ were used. The coefficients which correspond to Eqs. 1–2 are summarized in Table 1.
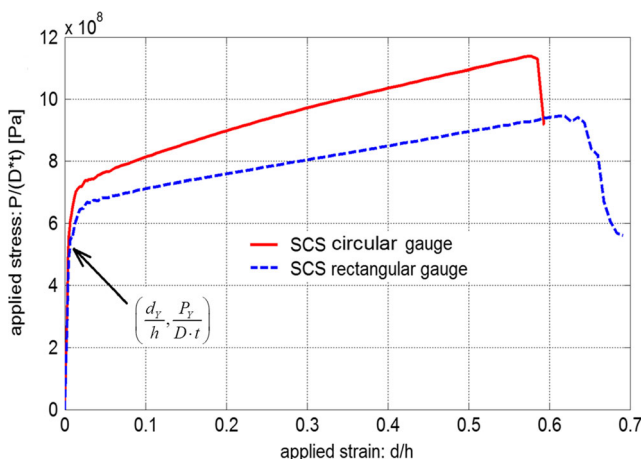

Fig. 8 Comparison of the applied normalized load–displacement curves for both types of specimen

Figure 12 shows the resulting approximations of $\sigma-\varepsilon_p$ with Eqs. 1–2 and coefficients of Table 1, together with the input to Abaqus, $\sigma-\varepsilon_p$. It can be observed that all 3 approximations replicate the input curve $\sigma-\varepsilon_p$ very well. A slightly better approximation is achieved for the rectangular gauge when two coefficients ($N=2$) are used with Eq. 6.

Experimental Results

The quasi-static tests are detailed in section 3.1 while the dynamic tests are detailed in section 3.2.

Quasi-Static Tests

All specimens were manufactured from cold drawn round steel bars C22E (DIN) or 1020 (AISI/SAE) having a diameter of 12 [mm]. The material was tested in the as-received ondition. Dog-bone, cylindrical, and both types of SCS specimens were machined.

The cylinders and SCS specimens were sandwiched between loading rods and compression was applied, while the dog-bone specimens were tested in tension. All specimens were tested quasi-statically on a servo-hydraulic MTS machine (model X) with a crosshead speed of 1 [mm/min]. The vertical displacements were measured with an optical laser extensometer, while force values were obtained from the load cell of the MTS machine. The tests stopped when the specimens deformed drastically or instability occurred. The dimensions of the dog-bone type and cylinder type specimen are shown in Fig. 13, and the dimensions of the circular and rectangular gauge SCS are given in Figs. 1 and 5 respectively. The average results of $\varepsilon_p-\sigma$ of five cylindrical specimens, four dog-bone, three rectangular SCS and four circular SCS are shown in Fig. 14. The results of both types of SCS specimens were obtained with the aid of the data reduction technique detailed in section 2.4. The SCS results will be validated numerically in the next section.

A very good agreement can be observed between all types of specimens regarding the large strain flow behavior especially for $0.15 < \varepsilon_p > 1.0$. It can be observed that the pressure effect in quasi-static loading is negligible, since the tensile dog-bone yields results that are similar to those of the compression cylinders. The cylinders and the SCS specimens had the same diameter (10 [mm]). The cylinders could characterize the steel up to strain of $\varepsilon_p=0.5$. The rectangular SCS could do it up to $\varepsilon_p=0.7$, while the circular SCS could do it up to $\varepsilon_p=1.0$. Such an observation was predicted by the numerical simulations reported in section 2.3.

Dynamic Tests

The cylindrical and both types of SCS specimens were tested in a Kolsky (SHPB) apparatus [26]. The averaged $\varepsilon_p-\sigma$

Fig. 9 Illustration of the generalized compression case: $\mu=1 \Rightarrow \sigma_1=\sigma_2$ for the case $\sigma_1, \sigma_3 > 0$
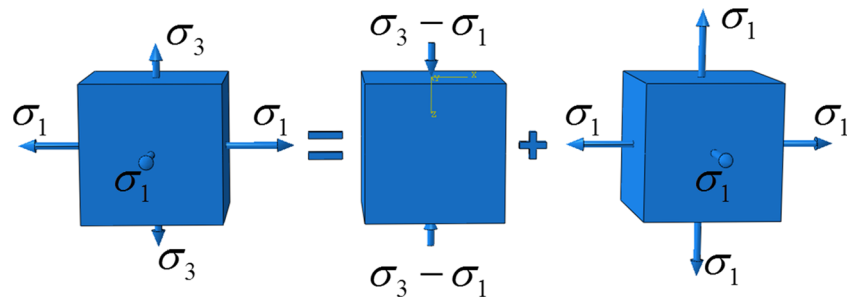
results of 5 cylinders, 5 circular and 4 rectangular SCS are shown in Fig. 15. All the results (not just the average) are detailed in Appendix A. It can be observed that for low plastic strains ($\varepsilon_p < 0.3$) both SCS results oscillates due to inertial effects. These oscillations could be smoothed [3]. In that regime the results obtained by cylinders give more reliable results. For larger plastic strain ($\varepsilon_p > 0.3$) there is a good agreement between the results obtained by both types of SCS. While the rectangular SCS could characterize the flow behavior up to $\varepsilon_p = 0.56$, the circular SCS reached $\varepsilon_p = 0.73$.

The average strain rate of the cylinders, SCS rectangular gauge, SCS circular gauge is 1960, 6110, and 9360 [1/s] respectively. The strain rate for the SCS specimens was calculated from the time derivative of the equivalent plastic strain on the mid section Eq. 6.

The results obtained for the SCS by using the data reduction technique (which was developed for quasi-static regime) *must be validated numerically*. This is done in the next sections.

All the dynamically tested SCS fractured in the gauge section, as expected. The two types of SCS specimen prior to testing are shown in Fig. 16 a and b. The dynamically fractured rectangular specimen is shown in Fig. 16c. It can be observed that the fracture occurred in the gauge fillet where stress concentration exist due to the 90° edge. The fractured circular specimen is shown in

Fig. 16d. By contrast, fracture of the circular SCS did not occur in the fillet and propagated roughly at mid-height of the gauge.

Numerical Validation

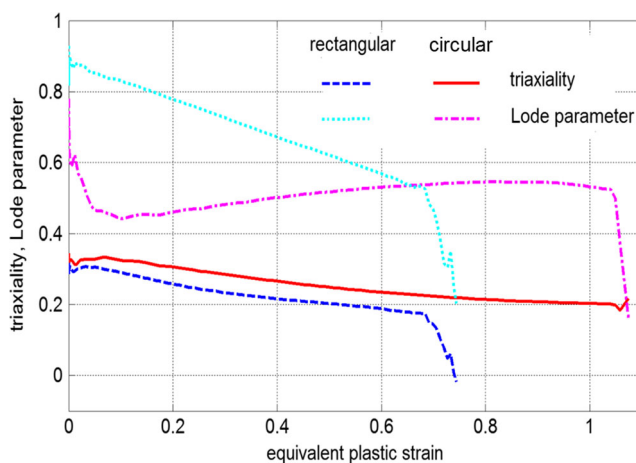The quasi-static and the dynamic tests of the SCS specimens were simulated numerically for validation purposes.

(a)

(b)

Fig. 11 **a**. Variation of the averaged plastic strain (ε_p) in the mid-cut section of the gauge with the applied normalize displacement ($\frac{d}{h}$). **b**. Variation of the averaged Mises stress (σ) in the mid-section of the gauge with the applied normalized load ($\frac{P}{D \cdot t}$)

Fig. 10 Variation of the averaged triaxiality and Lode parameter along the mid-cut section during plastic deformations for both types of specimen
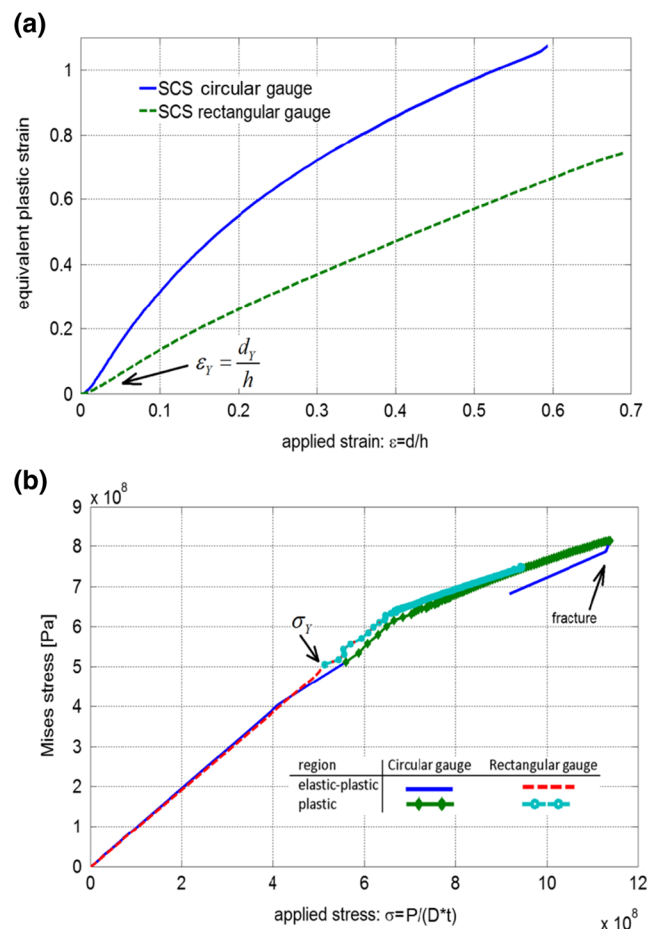
Table 1 Coefficient for data reduction

N	Circular gauge	Rectangular gauge	
	3	1	2
k_1	0.93	0.98	0.98
k_2	0.23	0.28	0.28
k_3	3.40	1.08	1.32
k_4	−3.73	–	−0.35
k_5	1.80	–	–

Validation of the Quasi-Static Tests

The numerical details are presented in section 2.2. Both types of SCS specimens were validated numerically using a trial and error procedure. The numerical validation involves application of displacement and calculation of the load which is required to apply the displacement. A validated $\varepsilon_p-\sigma$ curve is the one for which the numerically obtained d-P curve coincides with the experimentally measured d-P curve. Convergence means that the material property $\varepsilon_p-\sigma$ is correct. Results from the trial and error procedure are shown in Fig. 17 for the circular gauge SCS. A "first guess" for the $\varepsilon_p-\sigma$ was based on the experimental results shown in Fig. 14. It is shown in Fig. 17 that the d-P curve which resulted from this "first guess" is considerably higher than the three measured d-P test results. A "second guess" in which the flow stress was 10 % lower was used. The resulted d-P curve was slightly lower than the experimental d-P one. A "third guess" in which the flow stress was 7 % lower than the first guess was then used. It can be observed in Fig. 17 that a very good agreement exists between the numerical and experimental d-P curves. The "third guess" is considered as converged, and the corresponding $\varepsilon_p-\sigma$ represents the material property.
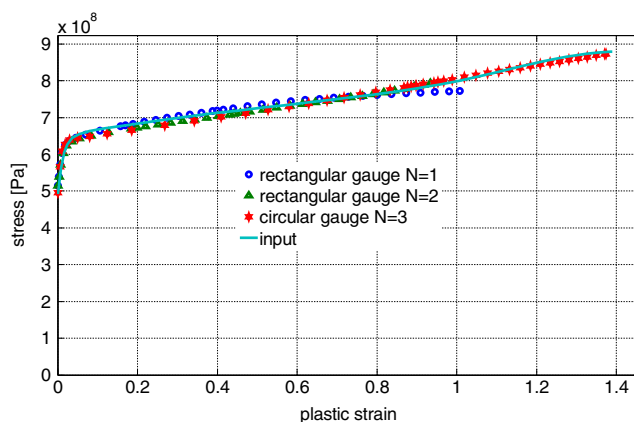
Fig. 12 Comparison between the approximations of $\sigma-\varepsilon_p$ with Eqs. 1–2 and coefficients of Table 1 to the input of Abaqus $\sigma-\varepsilon_p$

The converged $\varepsilon_p-\sigma$ curves for both types of SCS as well as the "first guess" which represents the experimental results shown on Fig. 14 are shown in Fig. 18. The "first guess" represents basically the cylindrical specimens' results for which the Lode parameter equals 1 ($\mu=1$). The flow stresses of the rectangular gauge SCS are 3 % lower and the flow stresses of the circular gauge SCS are 7 % lower. These small differences might be due to the difference in the value of the Lode parameter which is shown in Fig. 10. The lower the Lode parameter the lower the flow stress, as reported in [22].

Validation of the Dynamic Tests

Numerical Model, Mesh and Boundary Conditions

The numerical model included 3 parts: 1) Half of the incident bar. 2) The SCS specimen. 3) The transmitted bar. The assembly of these parts is shown in Fig. 19a. The specimen was aligned with the bars as shown Fig. 19b. Because of symmetry only half of the three parts above were modeled, as shown in the cut section of Fig. 19c.

The model uses a total number of 311,620 linear hexahedral elements of type C3D8R. The half incident bar, the SCS specimen and the transmitted bar has 109,080, 79,320 and 123,220 elements. The mesh is shown in Fig. 19b. The mesh size in the SCS gauge region is ~0.2 [mm] and on the bars ~1 [mm].

Symmetry conditions were applied all along the assembly on the face shown in Fig. 19c. Frictional contact conditions were applied between the SCS bottom and top face and the incident pulse bar and transmitted pulse bar (accordingly). A coefficient of friction 0.1, which corresponds to lubricated metal surfaces was used. The load was applied at the right end of the half incident bar. At that location in the experimental setup, a strain gauge is used to measure the incident and reflected pulses. The measured incident strain pulse multiplied by the Young's modulus of the bars was applied as a pressure. The pressure variation and its digitation for the validation of the circular gauge specimen are shown in Fig. 20.

Material Models and Properties

Elastic material model was used for the SHPB which are made of C300 maraging steel (Table 2). An adiabatic elastic-plastic material model was used for the 1020 steel (Table 2). The stress-plastic strain curve which was input into Abaqus for the rectangular and circular gauges is shown in Fig. 21. The experimental plastic strain results of the circular gauge SCS reach a value of $\varepsilon_p=0.73$ while the rectangular reaches $\varepsilon_p=0.56$. The purpose of the analysis is to validate the stress–strain results in these regimes.

A ductile failure criterion [27] was used. An element failed when the equivalent plastic strain reached a value of 2.5. A displacement type damage evolution [27] of 10 [μm] was

Fig. 13 Geometry and dimensions of the cylindrical and dog-bone specimens. All dimensions in [mm]
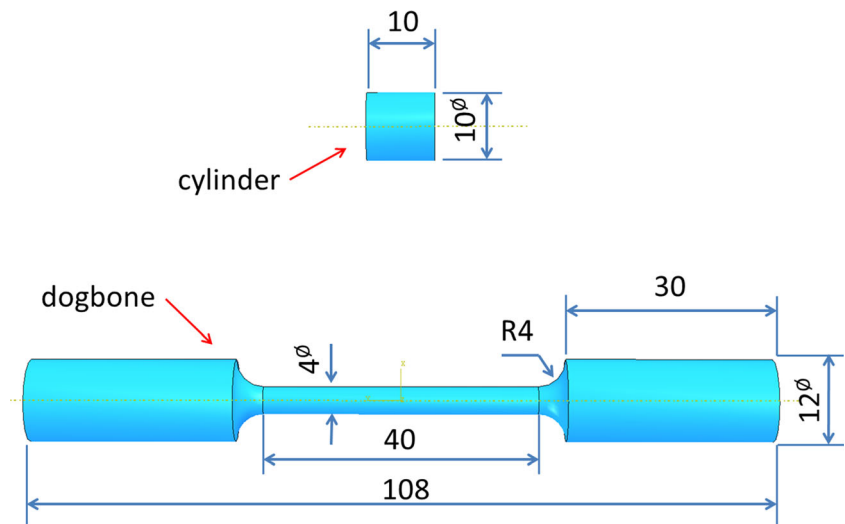
used. These values were used because they yield a good agreement between the experimental and the calculated transmitted interfacial forces.

Numerical Results

Figure 22a shows a comparison between the experimental and numerical results for F_{out}, the interfacial transmitted force, of the rectangular SCS, while Fig. 22b does it for the circular SCS. The $\sigma-\varepsilon_p$ curves which were used for each SCS type are shown in Fig. 21. A very good agreement can be observed for both types of specimens. Note that the numerical $\sigma-\varepsilon_p$ results are divided into two regions: 1) The region for which $\varepsilon_p<0.56$ for the rectangular gauge. 2) The region for which $\varepsilon_p<0.73$ for the circular gauge. For the small plastic strains (up to $\varepsilon_p=0.56$ for the rectangular gauge and up to $\varepsilon_p=0.73$) the $\sigma-\varepsilon_p$ input was according to the experimental results shown in Fig. 15, with an extrapolation at larger strains in excess of $\varepsilon_p=2.5$. The

behavior of $\sigma-\varepsilon_p$ at large plastic strain as well as the failure strain and the damage evolution values were all chosen to fit the experimental F_{out} results.

The results indicate that there is a difference of ~8 % between the characteristic flow stress obtained with the circular SCS and the rectangular one, with the first being lower. The reason might be the difference in the triaxiality and/or Lode parameter during the plastic deformation, as reported in [23].

The Lode parameter is associated with the third stress invariant of the stress deviator. The classical J2 theory of metal plasticity assumes that the plastic flow is independent of the hydrostatic stress and the Lode parameter, but recent experiments on metals [22] have shown that both the effects of pressure and the third deviatoric stress invariant (Lode parameter) should be included in the constitutive description of metals.

The variation of the averaged t_r and μ along the mid-section of both types of SCS specimens during plastic deformation are shown in Fig. 23. The average values during plastic strain
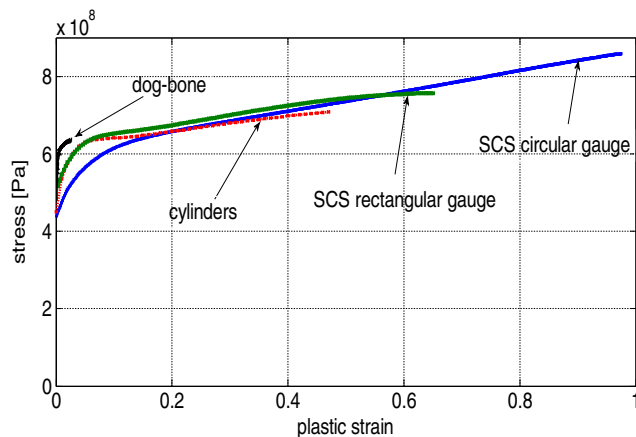

Fig. 14 Averaged flow stress vs. plastic strain obtained by dog-bone (tension), cylinders and both types of SCS (compression)
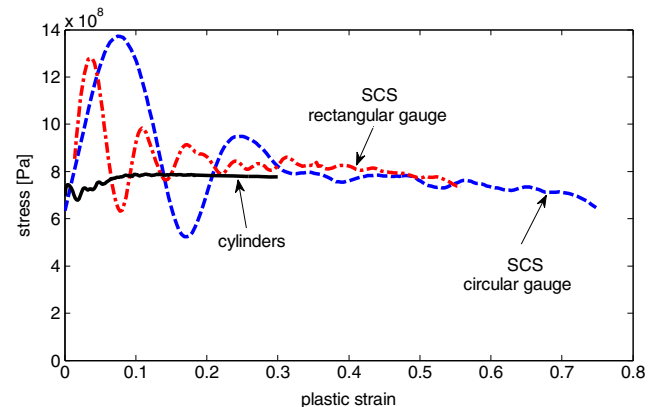

Fig. 15 Averaged flow stress vs. plastic strain obtained by cylinders and both types of SCS
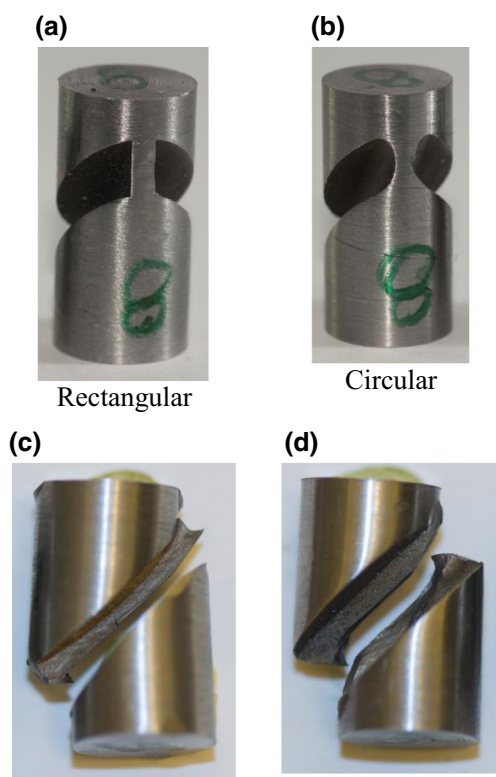
Fig. 16 SCS specimens prior and after testing in a SHPB. **a**. Rectangular type SCS prior to impact. **b**. Circular type SCS prior to impact. **c**. Side views of a broken rectangular type SCS. Note that the fracture propagated entirely along the fillet. **d**. Side views of a broken circular type SCS. Note that the fracture propagated roughly at mid-height of the gauge. The fracture paths compare very well with those shown in Fig. 6

variation $0 \leq \varepsilon_p \leq 0.7$ are : $t_r = 0.28$ and $\mu = 0.77$ for the rectangular SCS, and $t_r = 0.36$ and $\mu = 0.53$ for the circular SCS. While the triaxiality variation in both types of specimens is similar, the variation of Lode parameter is not. The μ variation in the circular gauge specimen is significantly lower. Lower positive values of μ mean that the stress situation is getting closer to a
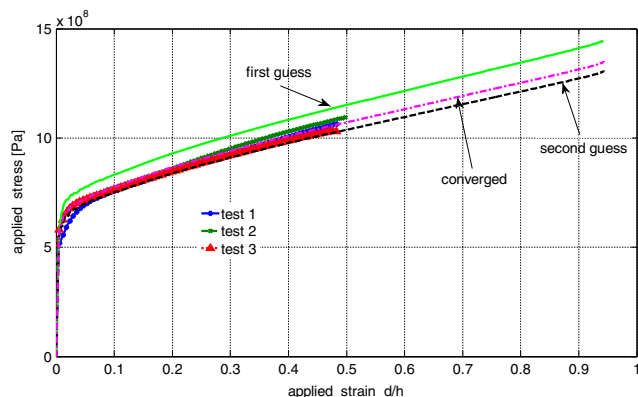

Fig. 17 Experimental and numerically calculated load–displacement *curves* for various stress–strain curves showing the "trial and error" process
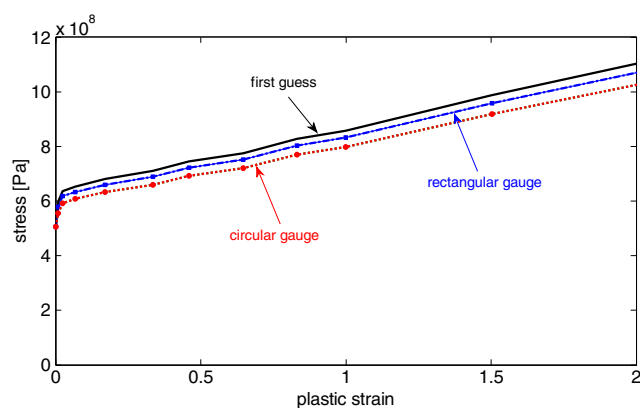

Fig. 18 Characteristic stress–strain *curves* for steel 1020 loaded quasi-statically obtained by using cylindrical specimens, together with rectangular and circular SCS

state of generalized shear while higher positive values means that the stress situation is closer to general compression.

Summary and Conclusions

The Shear Compression Specimen has been used and validated in many instances. While many meaningful results have been obtained with this specimen, there is a clear need to overcome one main limitation, and to revisit the specimen itself in terms of recent developments in the field of Solid Mechanics.

The limitation of the conventional SCS is due to the rectangular nature of its gauge, which inherently comprises stress concentration areas. Therefore, failure and fracture is always forced to occur in those regions. Since the stress concentration is very limited spatially to the fillets, it is not a real limitation for the determination of stress–strain characteristics of a material, over a large range of strains and strain-rates in a seamless manner, as stated in the original presentation of the specimen. However, there is always a need to characterize more mechanical parameters, one of them being the ductility to failure of a given material.

Using a combination of experimental tests and numerical simulations, a new gauge shape, semicircular, has been shown to seriously reduce the influence of the stress concentrations in the rectangular fillets, so that a marked increase in range of characterized plastic strain (not ductility) could be achieved in the experimental tests. This, in itself, is a very consequent achievement for the determination of failure strains. In addition, the new location of the failure path opens also new perspectives for experiments with adiabatic shear banding and real time thermal measurements, not to mention high speed imaging.

The Mechanics community has recently manifested a renewed interest in the issues of stress-triaxiality and Lode parameter. The conventional rectangular SCS design was

Fig. 19 The model assembly which was used for the numerical validation. **a**. The assembly. **b**. Magnification of the specimen area showing the mesh. **c**. A cut section through the model showing the face on which symmetry condition were applied
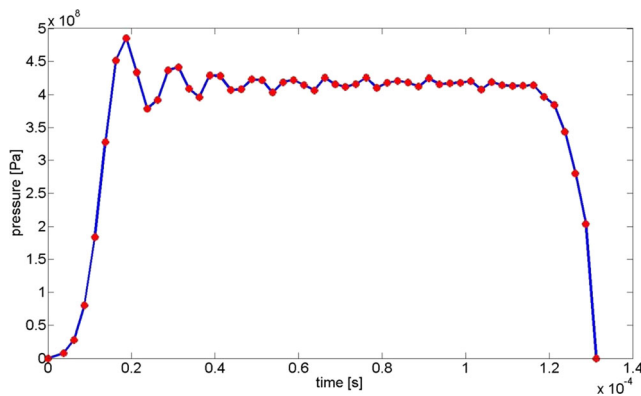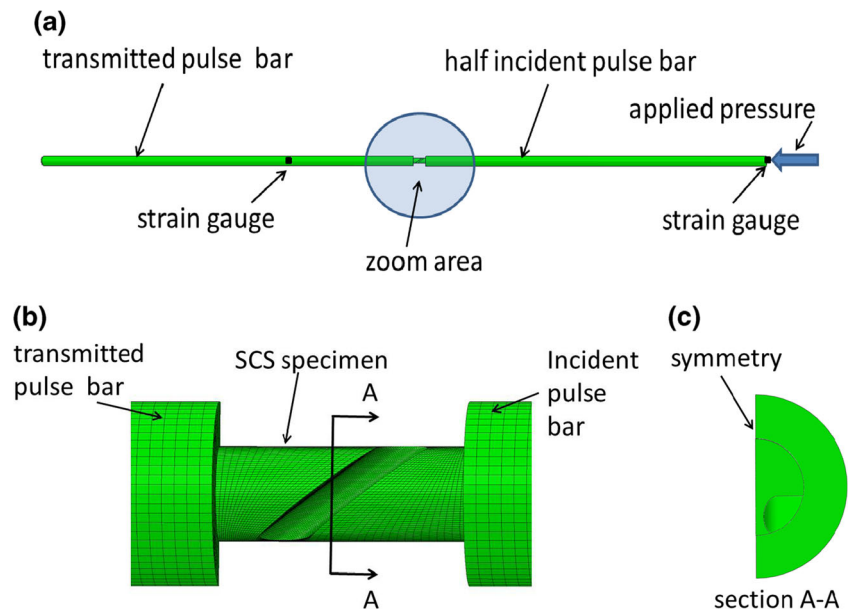

Fig. 20 The applied pressure

not the case for the former design. This too opens interesting perspectives in the characterization of the mechanical properties with emphasis on stress triaxiality and Lode parameter.

Finally, one more point should be mentioned, which will be the subject of a coming paper. Namely, while shear-compression tests have become almost routine testing with the SCS, *shear-tension tests* are almost never carried out for the lack of proper specimens to achieve that state of stress. The adaptation of the new circular SCS design for such tests should be carried out.

Therefore, the conclusion of the present work regarding the new gauge circular design of the SCS can be formulated as follows:

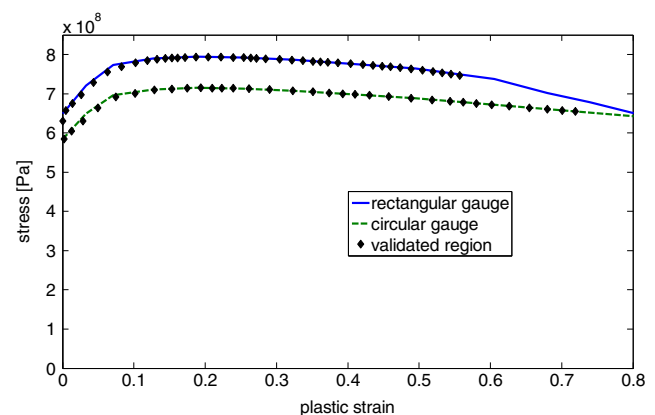- The failure locus occurs now at mid-gauge height as opposed to the fillets.

shown previously to have a relatively homogeneous distribution of its hydrostatic stress component in the gauge section. The new cylindrical SCS design shows the same property. But the numerical simulations shown in the present work show one more advantage of the new SCS design, namely a relatively homogeneous and constant Lode parameter, which was

Table 2 Material properties

	Steel 1020	Maraging steel
Density ρ $\left[\frac{Kg}{m^3}\right]$	7870	8000
Young's modulus E [GPa]	210	185
Poison's ratio ν	0.3	0.3
Inelastic heat fraction	0.9	–
Specific heat $\left[\frac{J}{Kg\,C^{-}}\right]$	486	–

Fig. 21 stress–strain plastic flow which was input to Abaqus
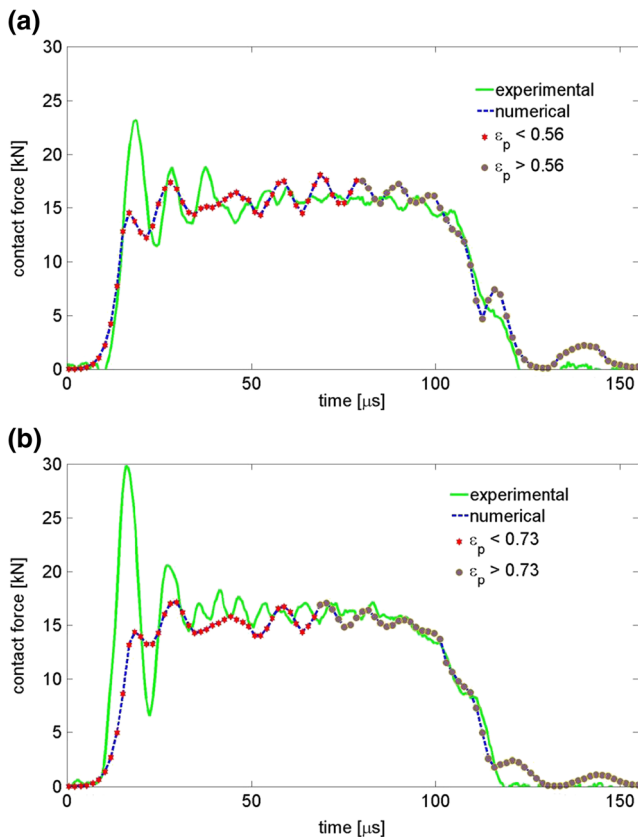
(a)

(b)

Fig. 22 Calculated transmitted interfacial force (F_{out}). **a**. Rectangular gauge. **b**. Circular gauge

- The resulting characterized plastic strain increase significantly with the new design.
- Both the stress-triaxiality and Lode parameter are homogeneous and rather constant in the new circular SCS.

Those characteristics pave the way for additional reliable characterization of the mechanical properties of materials.
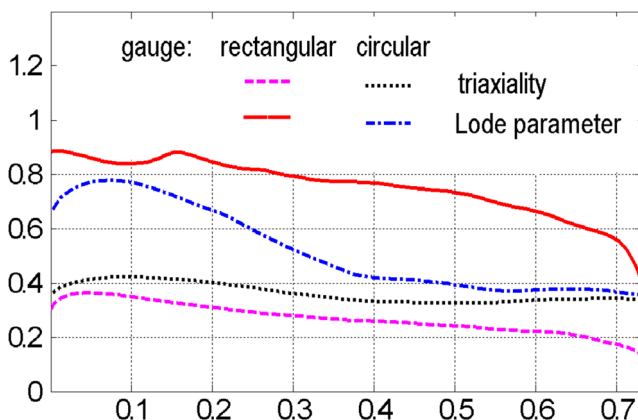

Fig. 23 The variation of the averaged t_r and μ along the mid cut section of both types of SCS specimens during plastic deformation

Appendix

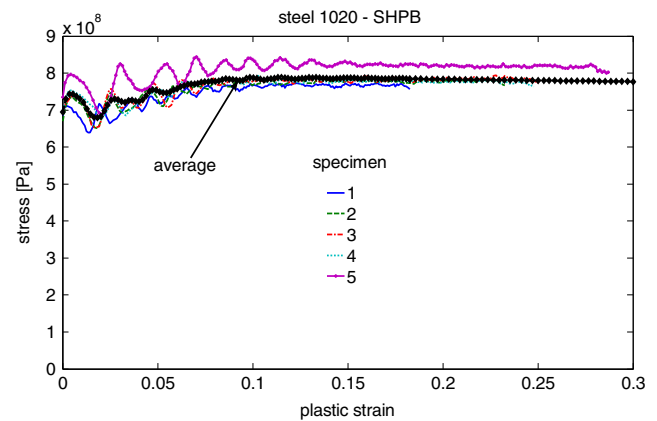Detailed dynamic experimental results.

Fig. 24 Stress–strain results of five cylindrical specimens impacted in a SHPB. The average strain–stress *curve* which was used in the text is emphasized
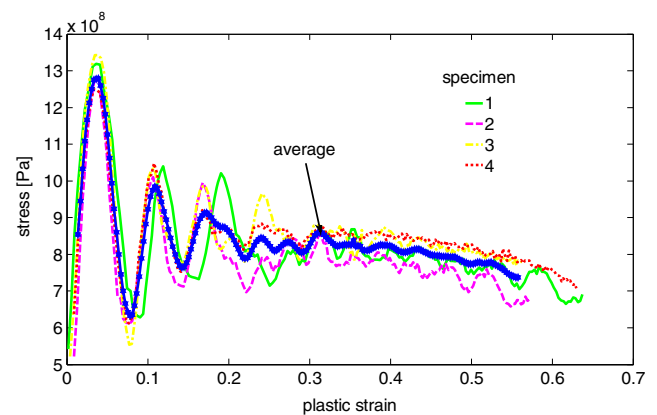

Fig. 25 Stress–strain results of four rectangular gauge SCS's impacted in a SHPB. The average strain–stress curve which was used in the text is emphasized
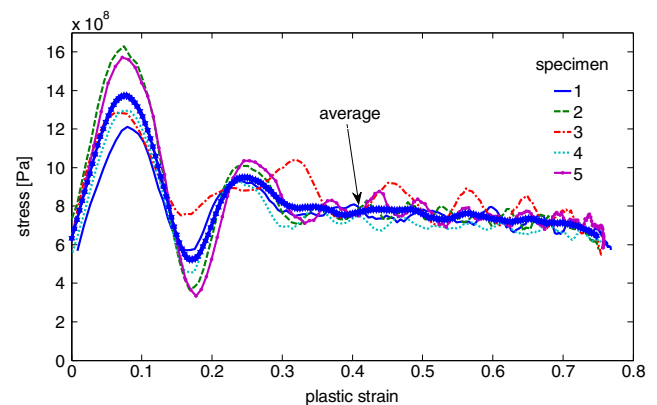

Fig. 26 Stress–strain results of five circular gauge SCS's impacted in a SHPB. The average strain–stress curve which was used in the text is emphasized

References

1. Rittel D, Lee S, Ravichandran G (2002) A shear compression specimen for large strain testing. Exp Mech 42:58–64

2. Dorogoy A, Rittel D (2005) Numerical validation of the Shear Compression Specimen (SCS). Part I: Quasi-static large strain testing. Exp Mech 45:167–177

3. Dorogoy A, Rittel D (2005) Numerical validation of the Shear Compression Specimen (SCS). Part II: Dynamic large strain testing. Exp Mech 45:178–185

4. Dorogoy A, Rittel D (2006) A numerical study of the applicability of the Shear Compression Specimen to parabolic hardening materials. Exp Mech 46:355–366

5. Rittel D, Lee S, Ravichandran (2002) Large strain constitutive behavior of OFHC copper over a wide range of strain-rates using the shear compression specimen. Mech Mater 34:627–642

6. Vural M, Rittel D, Ravichandran G (2003) Large strain mechanical behavior of 1018 cold-rolled steel over a wide range of strain rates. Metall Mater Trans A 34:2873–2885

7. Rittel D, Levin R, Dorogoy A (2004) On the isotropy of the dynamic mechanical and failure properties of swaged tungsten heavy alloys. Metall Mater Trans A 35:3787–3795

8. Bhattacharyya A, Rittel D, Ravichandran G (2005) Effect of strain rate on deformation texture of OFHC copper. Scr Mater 52:657–661

9. Rittel D, Wang ZG, Merzer M (2006) Adiabatic shear failure and dynamic stored energy of cold work. Phys Rev Lett 96(075502–1): 075502–075504

10. Rittel D, Wang ZG, Dorogoy A (2008) Geometrical imperfection and adiabatic shear banding. Int J Impact Eng 35:1280–1292

11. Rittel D, Wang Z (2008) Thermo-mechanical aspects of adiabatic shear failure of AM60 and Ti6Al4V alloys. Mech Mater 40:629–635

12. Ames M, Grewer M, Braun C, Birringer R (2012) Nanocrystalline metals go ductile under shear deformation Mater. Sci Eng A 546: 248–257

13. Zhao J, Knauss WG, Ravichandran G (2009) A new shear-compression-specimen for determining quasistatic and dynamic polymer properties. Exp Mech 49:427–436

14. Alkhader M, Knauss WG, Ravichandran G (2011) The influence of pressure on the large deformation shear response of a Polyurea. Conf Proc Soc Exp Mech Ser 3:287–295

15. Vural M, Molinari A, Bhattacharyya N (2011) Analysis of slot orientation in shear-compression specimen (SCS). Exp Mech 51: 263–273

16. Osovski S, Rittel D, Landau P, Venkert A (2012) Microstructural effects on adiabatic shear band formation. Scr Mater 66:9–12

17. Dolinski M, Rittel D, Dorogoy A (2010) Modeling adiabatic shear failure from energy considerations. J Mech Phys Solids 58:1759–1775

18. Abaqus, 2012. Finite element package, v6.12–2, Dassault Systemes, Simulia Corp., Providence, RI

19. Barsoum I, Faleskog J (2007) Rupture mechanisms in combined tension and shear -Experiments. Int J Solids Struct 44: 1768–1786

20. Bai Y, Wierzbicki T (2008) A new model of metal plasticity and fracture with pressure and Lode dependence. Int J Plast 24:1071–1096

21. Barsoum I, Faleskog J (2007) Rupture mechanisms in combined tension and shear - Micromechanics. Int J Solids Struct 44:5481–5498

22. Gao X, Zhang T, Hayden M, Roe C (2009) Effects of the stress state on plasticity and ductile failure of an aluminum 5083 alloy. Int J Plast 25:2366–2382

23. Keshavarz A, Ghajar R, Mirone G (2014) A new experimental failure model based on triaxiality factor and Lode angle for X-100 pipe line steel. Int J Mech Sci 80:175–182

24. Pivonka P, Willam K (2003) The effect of the third invariant in computational plasticity. Eng Comput 20:741–753

25. MATLAB R (2013b) The MathWorks Inc., Natick, MA 01760–2098, USA

26. Kolsky H (1949) An investigation of the mechanical properties of materials at very high rates of loading. Proc Phys Soc London 62-B: 676–700

27. Abaqus/CAE version 6.12-2 (2009). Abaqus documentation Abaqus analysis user's manual. Dassault systemes. Springer, New York, Chapter 24: Progressive Damage and Failure